Supporting Information

Spacer Ligands Govern the Charge Mobility and Luminescence in Mn-doped 2D Ruddlesden-Popper Perovskites

*Amar Nath Yadav[1], Du Chen[2, 3], Shunran Li[2, 3], Mikaël Kepenekian[4], Peijun Guo[2, 3], Ido Hadar[1]**

[1]*Institute of Chemistry, the Center for Nanoscience and Nanotechnology, and Casali Center for Applied Chemistry, the Hebrew University of Jerusalem, Jerusalem, 91904, Israel.*

[2] *Department of Chemical and Environmental Engineering, Yale University, New Haven, CT 06520, USA.*

[3]*Energy Sciences Institute, Yale University, West Haven, Connecticut 06516, USA.*

[4]*Univ Rennes, ENSCR, INSA Rennes, CNRS, ISCR (Institut des Sciences Chimiques de Rennes), UMR 6226, Rennes F-35000, France*

*Corresponding author email: ido.hadar@mail.huji.ac.il

This supporting information includes:

Section 1: Experimental section

S1. Materials

Phenethylammonium bromide (PEABr, greatcell solar materials), n-butylammonium bromide (BABr, 98%≥, sigma-aldrich), phenethylamine (99%, thermo fisher), butylamine (99%, holland moran), lead bromide ($PbBr_2$, 98%, thermo-scientific), lead oxide (PbO, 99.9%, alfa aesar), manganese bromide, N, N-Dimethylformamide (DMF, 99%, thermo fisher), Toluene (Bio Lab), hydrobromic acid (HBr, 48%, thermo fisher), hypophosphorous acid (H_3PO_2, thermo fisher). The chemicals were used as received, without undergoing any additional purification processes.

S2. Synthesis

S2.1 Synthesis of Mn-doped $(L)_2PbBr_4$ (L = PEA or BA) 2D perovskite nanoplatelets (NPLs)

The Mn-doped 2D lead bromide hybrid perovskite NPLs, with the formula $(L)_2[(Pb)_{1-x}Mn_x]Br_4$, were synthesized using the ligand-assisted reprecipitation (LARP) method, as previously described.[1] First, 0.20 M precursor solutions were prepared by dissolving LBr (L = PEABr or BABr), $PbBr_2$, and $MnBr_2$ in 1 mL of DMF, each separately in a vial. Since $PbBr_2$ and $MnBr_2$ do not dissolve readily in DMF, the solution was heated to 80°C for 10 minutes under stirring. The precursors were then mixed in ratios specified in **Table S1 (**with $PbBr_2$ and $MnBr_2$ mixed first, followed by the addition of LBr). After vortex mixing, the mixture was further heated for 1 minute at 80°C. The precursor solution was then cooled to room temperature, and a drop of it was injected into 10 mL of toluene under magnetic stirring. Within a few seconds, NPLs were formed and subsequently stored for further use.

S2.2 Synthesis of Mn-doped L_2PbBr_4 (L = PEA or BA) 2D perovskite crystals

The undoped and Mn-doped L_2PbBr_4 (L = PEA or BA) crystals were synthesized using the acid precipitation method, as previously reported.[2,3] For the typical synthesis of $(BA)_2Pb_{1-x}Mn_xBr_4$ (x = 0.5), PbO (2.5 mmol, 0.5580 g) and $MnBr_2$ (2.5 mmol, 0.5368 g) were added to 5 mL of HBr and 0.85 mL of H_3PO_2. The mixture was heated to 130°C under stirring until a clear solution was obtained. Meanwhile, 988 µL (10 mmol) of butylamine was added dropwise to 5 mL of HBr in a separate vial under an ice bath. This butylamine mixture was then added dropwise to the above salt-precursor solution. The temperature was subsequently increased from 130°C to 150°C to dissolve the resulting precipitate. The mixture was then slowly cooled to room temperature without further disturbance. During cooling, crystals were precipitated,

washed with ethanol, and vacuum-dried. Similarly, other crystals of $(BA)_2Pb_{1-x}Mn_xBr_4$ (x = 0, 0.70, 0.90) were synthesized using the same procedure.

For the synthesis of $(PEA)_2Pb_{1-x}Mn_xBr_4$ (x = 0–0.90) crystals, the same method was followed, with the only difference being that phenethylamine (200 µL) was added dropwise directly to the solution containing PbO, $MnBr_2$, HBr, and H_3PO_2, instead of being pre-mixed in HBr.

S3. Characterizations

S3.1 Optical characterizations

The UV-Vis absorption and photoluminescence (PL) spectra were measured using a UV-Vis-NIR JASCO spectrophotometer and a PL-RF6000 fluorescence spectrometer, respectively. As-synthesized colloidal NPLs in toluene were used to record these spectra. Low-temperature PL spectra were recorded on a home-built micro-spectroscopy setup. A laser with a wavelength of 371 nm and a repetition rate of 10 MHz was used to excite the samples. PLQY measurements were conducted on a Hamamatsu Absolute PL quantum yield spectrometer C11347-11. Raman spectroscopy was performed using a customized microscope-coupled spectrometer setup. A long working-distance objective lens (Mitutoyo, NIR, 20×, NA = 0.4) was employed to focus the 785 nm excitation light generated by a frequency-stabilized laser (Toptica) onto the sample. The resulting inelastically scattered Raman signal was gathered by the same objective and filtered using a series of five narrow-bandwidth, reflective volume Bragg grating notch filters (OptiGrate), enabling detection of Raman shifts as low as 5 cm^{-1}. The filtered signal was then directed through two 75 mm focal length achromatic lenses and a 50 µm pinhole before entering a spectrograph (Horiba iHR550, equipped with a 950 grooves/mm grating) and finally detected by a CCD camera (Horiba Syncerity).

S3.2 Structural characterizations

X-ray diffraction (XRD) patterns were recorded on a Bruker AXS D8 Advance X-ray powder diffractometer using Cu Kα radiation (λ = 1.5406 Å). Scanning transmission electron microscopy (STEM) imaging and energy-dispersive X-ray spectroscopy (EDS) mapping were conducted on an aberration-probe-corrected STEM Themis Z G3 (Thermo Fisher Scientific) setup operated at an accelerating voltage of 300 kV. The setup was equipped with a high angular annular dark field detector (HAADF) for STEM and a Super-X energy dispersive X-Ray spectroscopy (EDS) detector for high collection efficiency elemental analysis. The obtained images and EDS maps were analyzed with Velox software (Thermo Fisher Scientific). Inductively Coupled Plasma Mass Spectrometry (ICP-MS) was performed on the Agilent Technologies 8900 ICP-MS Triple Quad. For this measurement, the colloidal samples were

centrifuged and diluted at the ppb level in an aqueous solution of 1% HNO_3. Similarly, crystals were also diluted and measured.

S3.3 Cathodoluminescence (CL) measurement

CL measurements in a scanning electron microscope (SEM) were carried out on an Analytical High-Resolution SEM Apreo 2S (Thermo Fisher Scientific). The instrument was equipped with a SPARC system for CL spectroscopy and mapping. In this setup, an electron beam (with an operating voltage of 10 kV and a beam current of 3.2-6.4 nA) is directed onto the sample surface through an opening in a parabolic mirror. The stage height is carefully adjusted to position the light-emitting region of the sample at the mirror's focal point. This alignment is typically optimized by maximizing the intensity and symmetry of the detected signal. The emitted light, collected by the mirror, is then guided out of the SEM's vacuum environment and focused directly onto a light detector. For this measurement, as-synthesized colloidal NPLs were drop-cast onto a silicon substrate and dried at room temperature. The obtained data were analyzed with Odemis Viewer software (Delmic).

S3.4 Transient reflection microscopy (TRM) measurement for carrier diffusivity

A schematic illustration of our TRM setup is shown in **Figure S13A**. The pump light, centered at 640 nm, was generated using an optical parametric amplifier (OPA, Orpheus ONE) driven by a Pharos amplifier, which produces a fundamental output at 1030 nm with a pulse duration of 170 fs and a repetition rate of 2 kHz. A portion of this fundamental light was split and time-delayed using a mechanical delay stage, then focused onto a 4-mm-thick YAG crystal to generate broadband visible light. A bandpass (BP) filter centered at 575 nm with a 20 nm bandwidth was used to isolate near-monochromatic, off-resonance probe light. A f = 300 mm wide-field lens (WFL) focused the probe beam onto the back aperture of the objective, enabling wide-field illumination over an area of approximately 16 μm. The pump and probe beams were combined using a 50/50 beam splitter (BS) and directed into a long-working-distance objective (Mitutoyo G Plan Apo 50x, NA = 0.50) with 3.5 mm of glass correction. The pump beam was focused to a spot with a full width at half maximum (FWHM) of ~1.4 μm and excited the sample *via* two-photon absorption. The reflected probe light was collected through the same objective and focused onto the charged metal–oxide semiconductor (CMOS) camera (PixeLINK PL-D753) using an f = 400 mm tube lens, providing a total magnification of 100x (**Figure S13B**). A 550–600 nm bandpass filter was placed in front of the CMOS camera to block the reflected pump light and PL from the sample. The transient reflectance, $\frac{\Delta R}{R} =$

$\frac{R(t)-R(0)}{R(0)}$, was calculated at each camera pixel, where R (0) and R (t) are the reflectance values before and after pump excitation, respectively (**Figure S13C**). The presence of charge carriers induces contrast in the microscopy image through interferometric scattering, with the scattered intensity being directly proportional to the excited-state population density.[4] All measurements were performed at ambient temperature with the samples placed in a vacuum chamber.

The spatiotemporal distribution of charge carriers was extracted by azimuthally integrating the Gaussian-shaped contrast intensity in the imaging to obtain $I(r,t)$. Fitting a Gaussian distribution to $I(r,t)$ at each time point gives its standard deviation σ (**Figure S1D**). The mean-square-displacement (MSD) of the charge carriers can then be calculated as:

$$MSD(t) = \sigma(t)^2 - \sigma(0)^2$$

A diffusive-to-sub-diffusive transport scheme was adopted here to account for the two subsequent diffusion regimes: 1) a normal diffusive regime with linear $MSD(t)$ behavior, i.e., $MSD(t) = 2Dt$, where D is the diffusivity; 2) a defect-mediated sub-diffusive regime with sublinear behavior, i.e., $MSD(t) = 2Dt^{\alpha}$, where $\alpha < 1$.[5] The measured $MSD(t)$ were then fitted with the following equation:

$$MSD(t) = \begin{cases} 2Dt + c, & t \le t_{split} \\ 2D\left[\left(t - t_{split} + t_0\right)^{\alpha} + t_{split} - t_0^{\alpha}\right] + c, & t > t_{split} \end{cases}$$

t_{split} is the separation point between the diffusive and sub-diffusive regime, c is a small offset constant, α is the sub-diffusive exponent, and $t_0 = \alpha^{1/(1-\alpha)}$.

S3.5 Density Functional Theory (DFT) calculations

First-principles calculations are based on DFT as implemented in the SIESTA package.[6,7] The nonlocal van der Waals density functional of Dion et al., corrected by Cooper (C09), to correctly describe the inorganic-organic interplay.[8,9] Geometry optimizations are performed with a spin-restricted formalism, while the band structures are described, including spin-orbit coupling through the so-called off-site approach following the Hemstreet formalism.[10] Core electrons are described with Troullier-Martins pseudopotentials, while valence wave functions are developed over a double-ζ polarized basis set of finite-range numerical pseudoatomic orbitals.[11,12] An energy cutoff of 150 Ry for real-space mesh size has been used. The Brillouin zones are sampled using a using a 9×9×2 Γ-centered Monkhorst-Pack grid. Starting from the experimentally determined structure of both compounds, complete

optimization of cell vectors and atomic positions are optimized until forces are lower than 0.01 eV/Å. The Bulk modulus is determined by applying isotropic strains. The resulting variations of energy are fitted using the Murnaghan equation of states, leading to the value of the bulk modulus B_0.[13]

Section 2: Supplementary tables

Table S1. Synthesis protocol for Mn-doped 2D lead bromide hybrid perovskite $L_2Pb_{1-x}Mn_xBr_4$ (L = PEA or BA, x = 0−0.70) nanoplatelets

Sample No.	PEABr or BABr	$PbBr_2$	$MnBr_2$	x = Mn/(Mn + Pb)
1.	80 µl	40 µl	0 µl	0
2.	80 µl	35 µl	5 µl	0.12
3.	80 µl	30 µl	10 µl	0.25
4.	80 µl	25 µl	15 µl	0.37
5.	80 µl	20 µl	20 µl	0.50
6.	80 µl	16 µl	24 µl	0.60
7.	80 µl	12 µl	28 µl	0.70

Table S2: ICP-MS of $(PEA)_2Pb_{1-x}Mn_xBr_4$ (x = 0.12−0.70) nanoplatelets

Sample No.	Pb_{feed}	Mn_{feed} or x	Pb (%)	Mn (%)
2.	0.88	0.12	97.51	2.49
3.	0.75	0.25	96.68	3.32
4.	0.62	0.38	94.27	5.73
5.	0.50	0.50	81.77	18.23
6.	0.40	0.60	58.60	41.40
7.	0.30	0.70	52.95	47.05

Table S3. ICP-MS of $(BA)_2Pb_{1-x}Mn_xBr_4$ (x = 0.12−0.70) nanoplatelets

Samples No.	Pb_{feed}	Mn_{feed} or x	Pb (%)	Mn (%)
2.	0.88	0.12	97.88	2.12
3.	0.75	0.25	96.24	3.76
4.	0.62	0.38	93.09	6.91
5.	0.50	0.50	81.40	18.60

6.	0.40	0.60	59.20	40.80
7.	0.30	0.70	53.46	46.53

Table S4. ICP-MS of $(PEA)_2Pb_{1-x}Mn_xBr_4$ (x = 0.50−0.90) crystals

Samples No.	Pb_{feed}	Mn_{feed} or x	Pb (%)	Mn (%)
2.	0.50	0.50	99.930	0.070
3.	0.30	0.70	99.857	0.143
4.	0.10	0.90	99.708	0.292

Table S5. ICP-MS of $(BA)_2Pb_{1-x}Mn_xBr_4$ (x = 0.50−0.90) crystals

Samples No.	Pb_{feed}	Mn_{feed} or x	Pb (%)	Mn (%)
2.	0.50	0.50	99.930	0.031
3.	0.30	0.70	99.857	0.079
4.	0.10	0.90	99.687	0.313

Section 3: Supplementary Figures

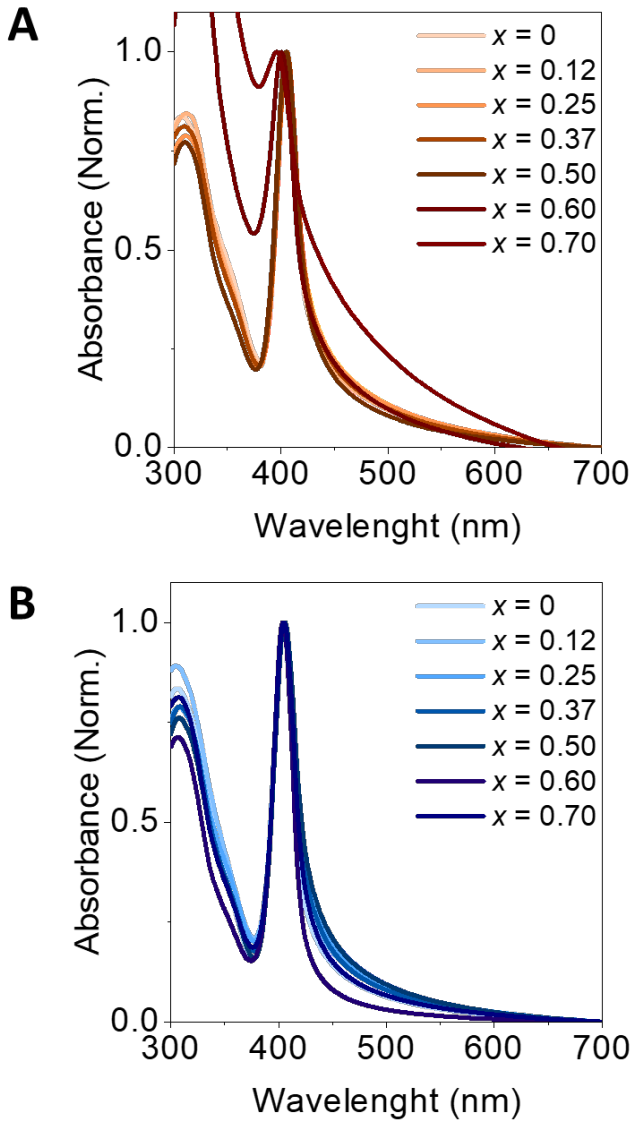

Figure S1. Absorption spectra of (A) $(PEA)_2Pb_{1-x}Mn_xBr_4$ and (B) $(BA)_2Pb_{1-x}Mn_xBr_4$ perovskite nanoplatelets with varying Mn-mole fraction (x = 0−0.70).

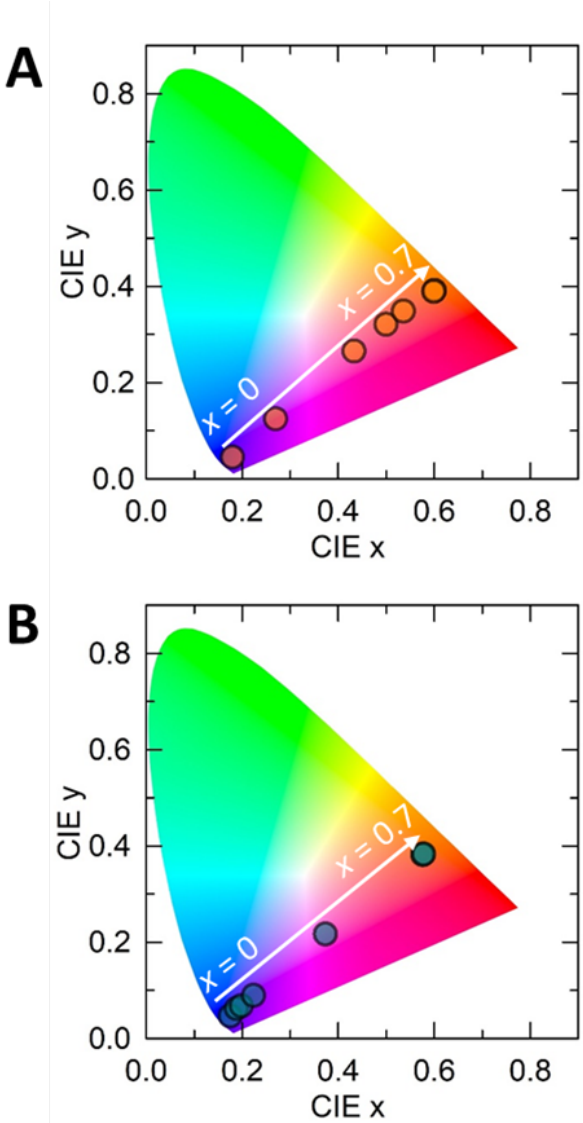

Figure S2. CIE color coordinate changes as a function of Mn mole fraction (x), ranging from 0 to 0.70, for (A) $(PEA)_2Pb_{1-x}Mn_xBr_4$ and (B) $(BA)_2Pb_{1-x}Mn_xBr_4$ perovskite nanoplatelets.

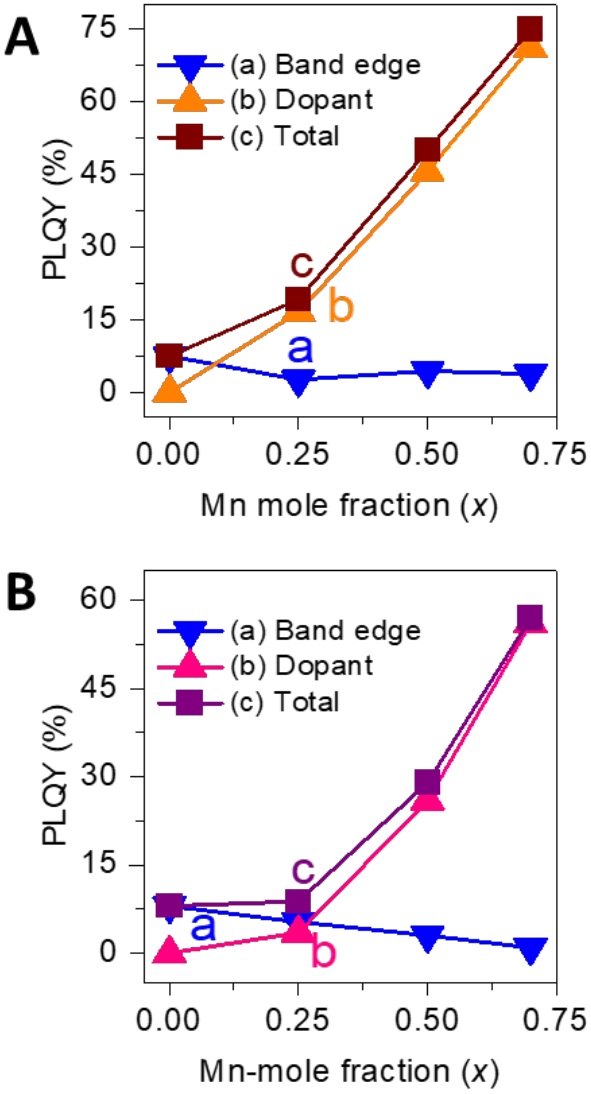

Figure S3. PLQYs of (A) $(PEA)_2Pb_{1-x}Mn_xBr_4$ and (B) $(BA)_2Pb_{1-x}Mn_xBr_4$ perovskite nanoplatelets with varying Mn-mole fraction (x = 0−0.70).

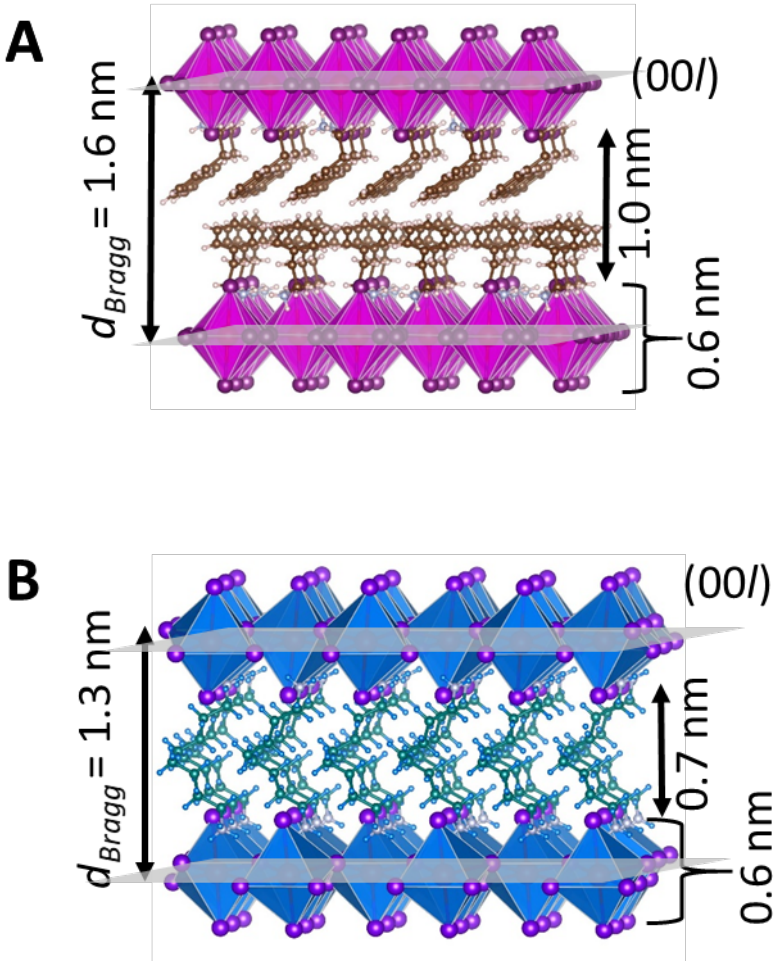

Figure S4. Schematic diagram of the crystal structure of (A) $(PEA)_2PbBr_4$ and (B) $(BA)_2PbBr_4$ perovskites, where the length of spacer ligands was calculated using the periodicity of the diffraction planes. The Vesta software is used to draw these structures using their CIF files.

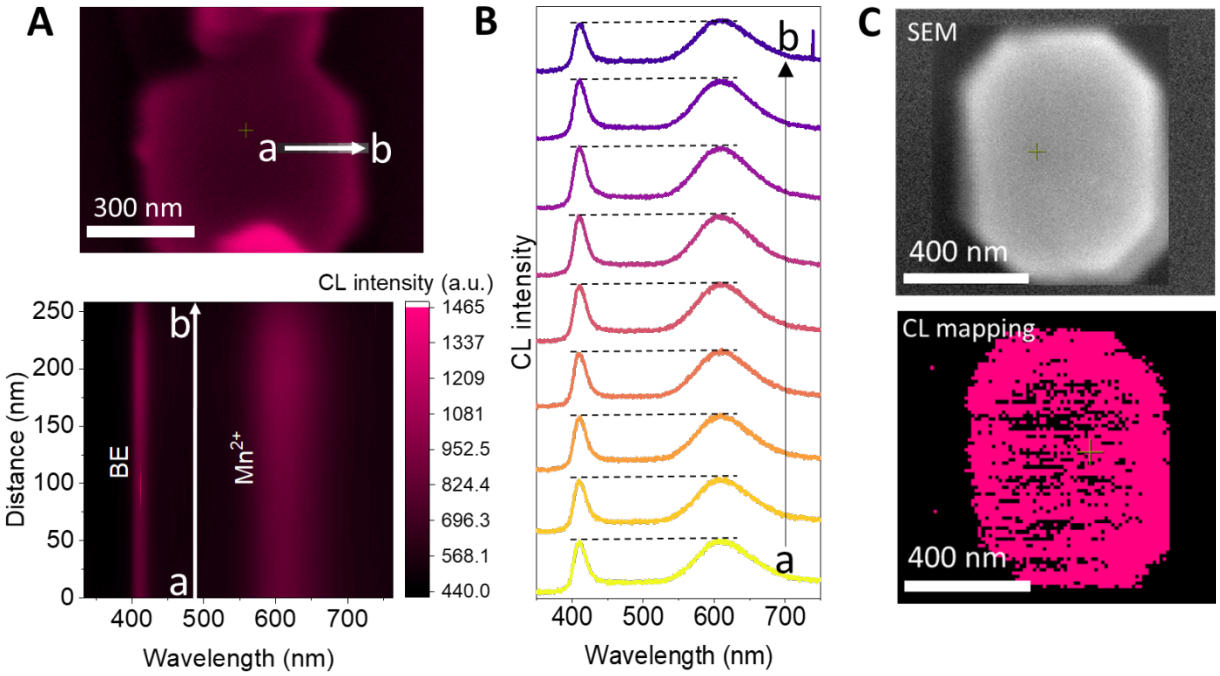

Figure S5. (A) SEM image (top) and 2D CL color map (bottom) (where scanning was performed from center to edge), (B) CL spectra for center to edge scan, and (C) SEM image (top) and CL mapping (bottom) of $(PEA)_2Pb_{1-x}Mn_xBr_4$ nanoplatelet at low doping $x = 0.37$.

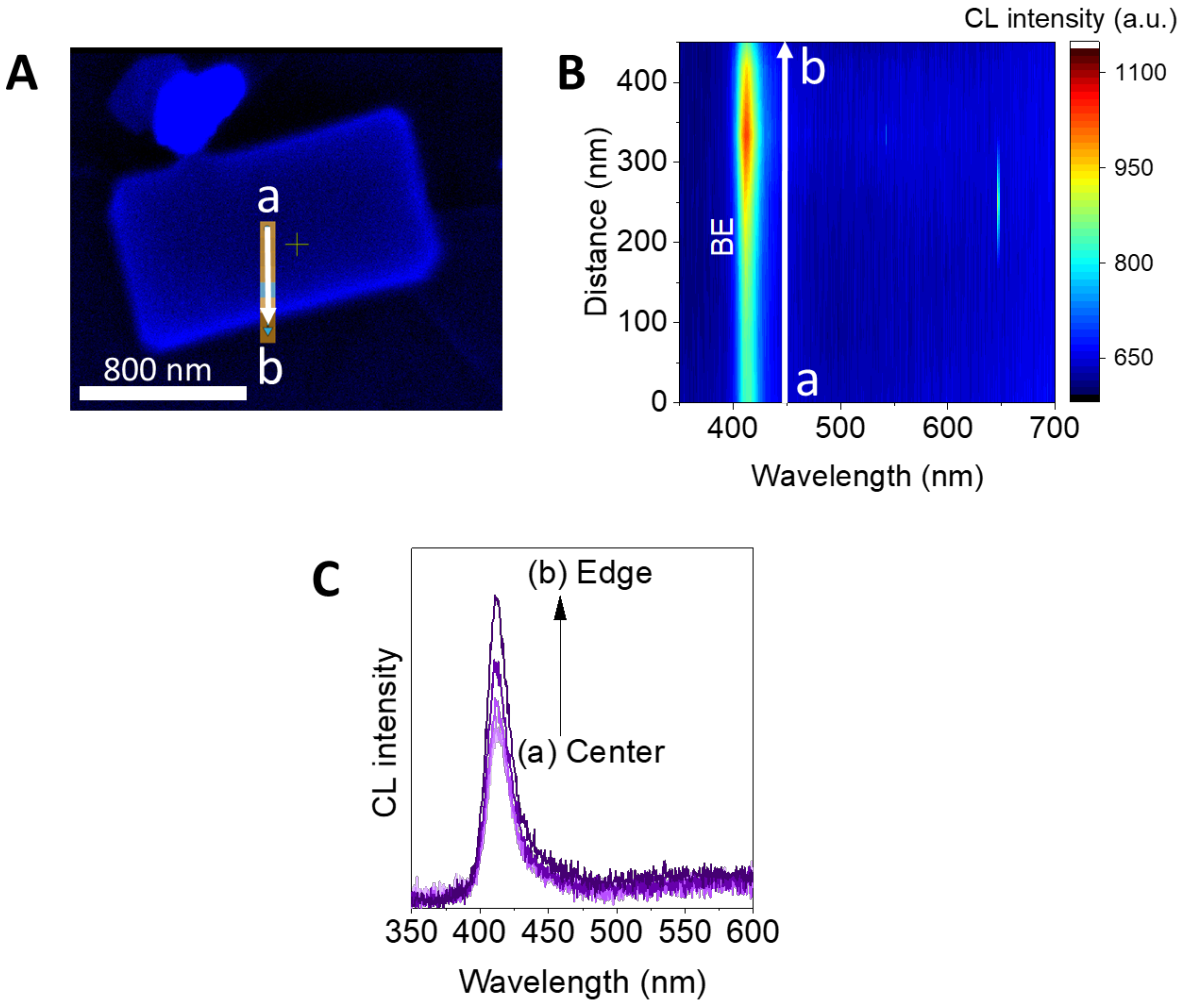

Figure S6. (A, B) SEM images (left) and 2D CL color maps (right) (where scanning was performed from center-to-edge. (C) CL spectra corresponding to the center-to-edge scan of $(PEA)_2PbBr_4$ nanoplatelet.

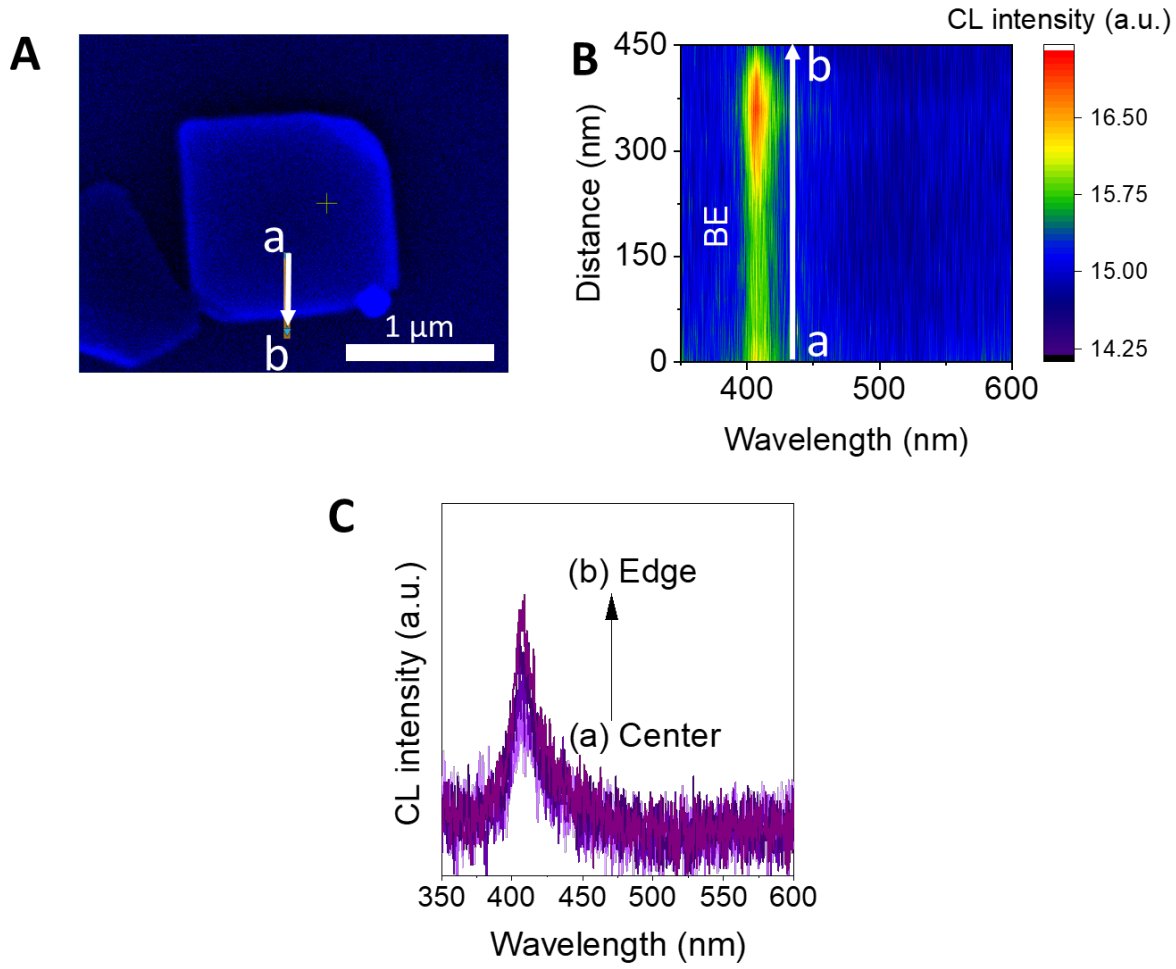

Figure S7. (A, B) SEM images (left) and 2D CL color maps (right) (where scanning was performed from center-to-edge. (C) CL spectra corresponding to the center-to-edge scan of $(BA)_2PbBr_4$ nanoplatelet.

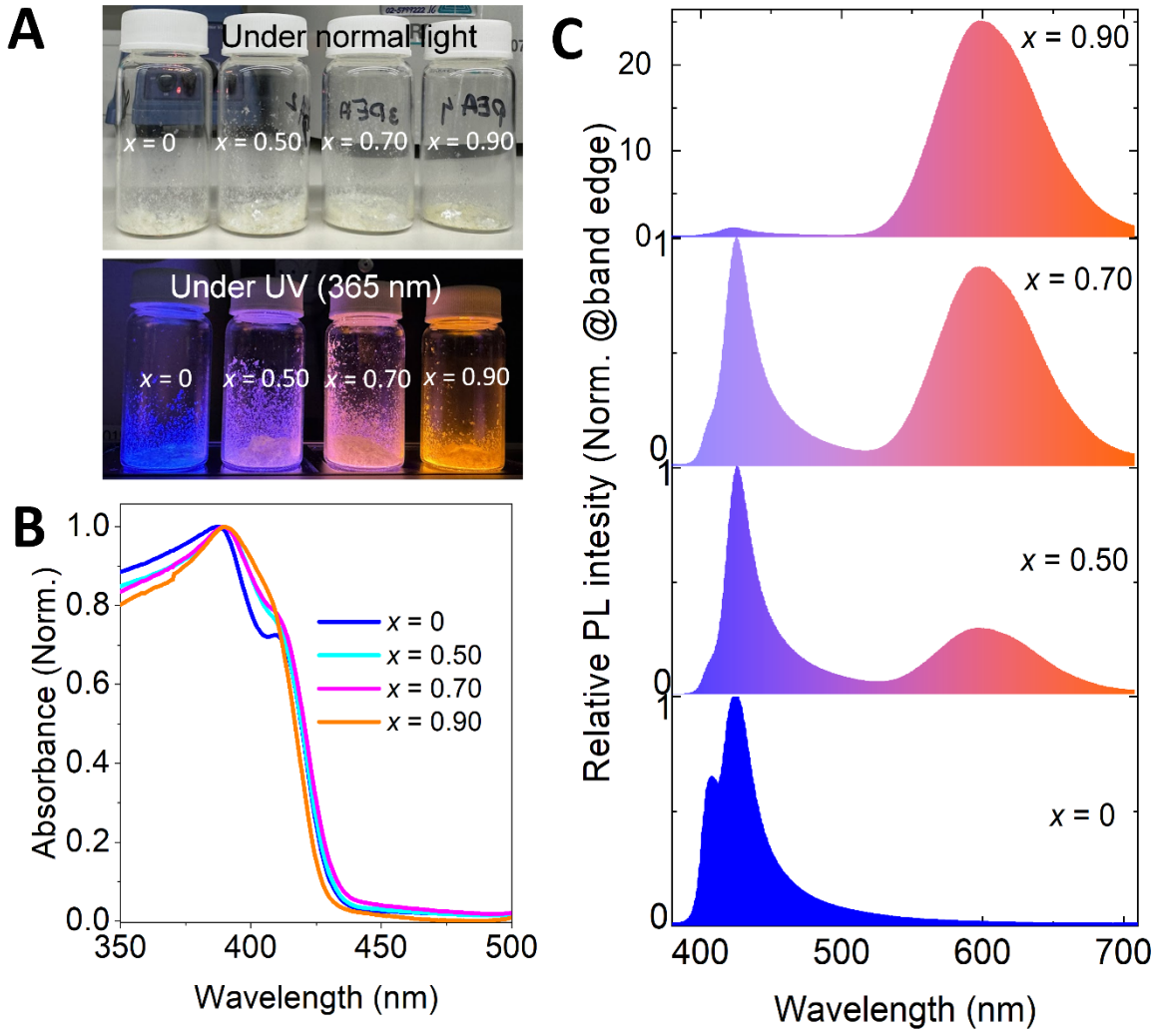

Figure S8. (A) Photographs of $(PEA)_2Pb_{1-x}Mn_xBr_4$ (x = 0−0.90) crystals under normal light and UV (365 nm). (B) Absorption spectra and (C) PL spectra of $(PEA)_2Pb_{1-x}Mn_xBr_4$ crystals, where x varied from 0 to 0.90.

.

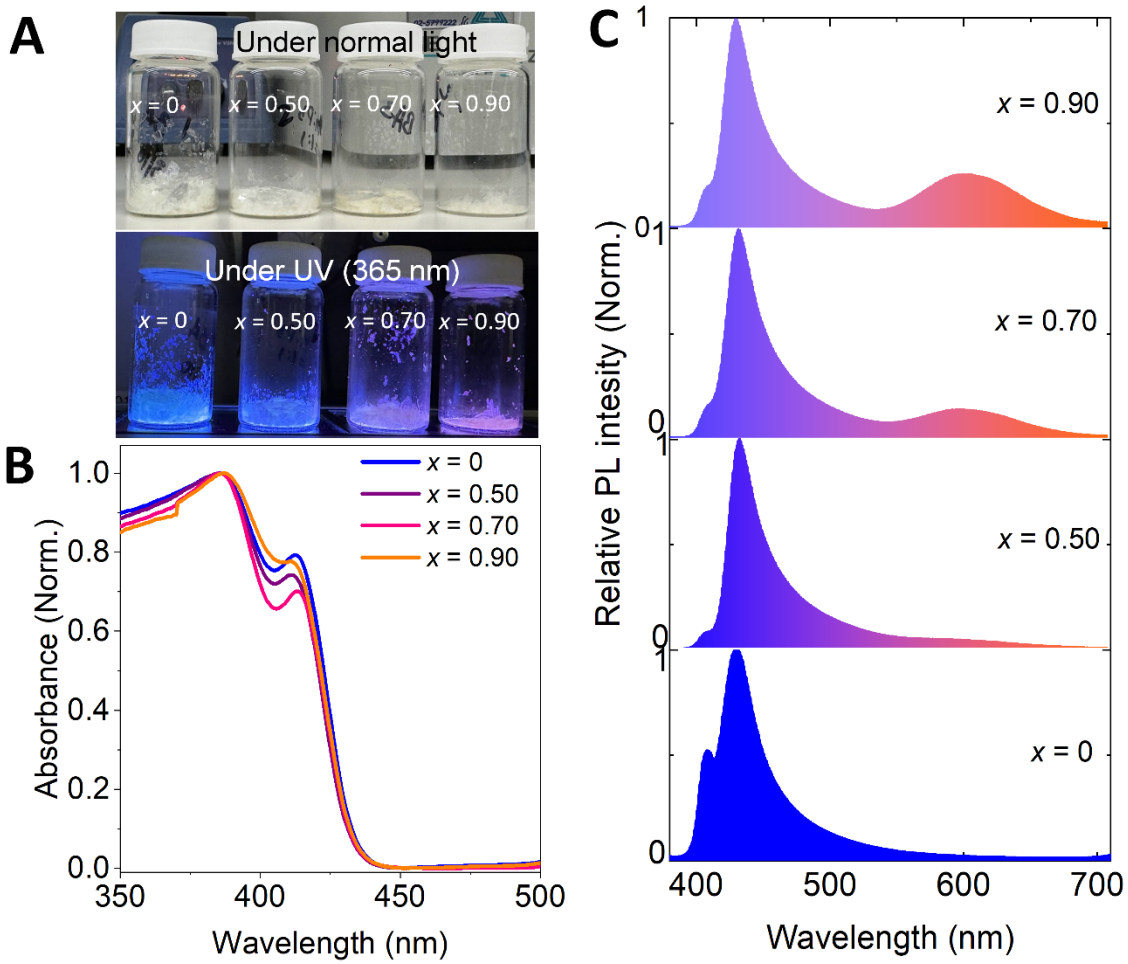

Figure S9. (A) Photographs of $(BA)_2Pb_{1-x}Mn_xBr_4$ (x = 0−0.90) crystals under normal light and UV (365 nm). (B) Absorption spectra and (C) PL spectra of $(BA)_2Pb_{1-x}Mn_xBr_4$ crystals, where x varied from 0 to 0.90.

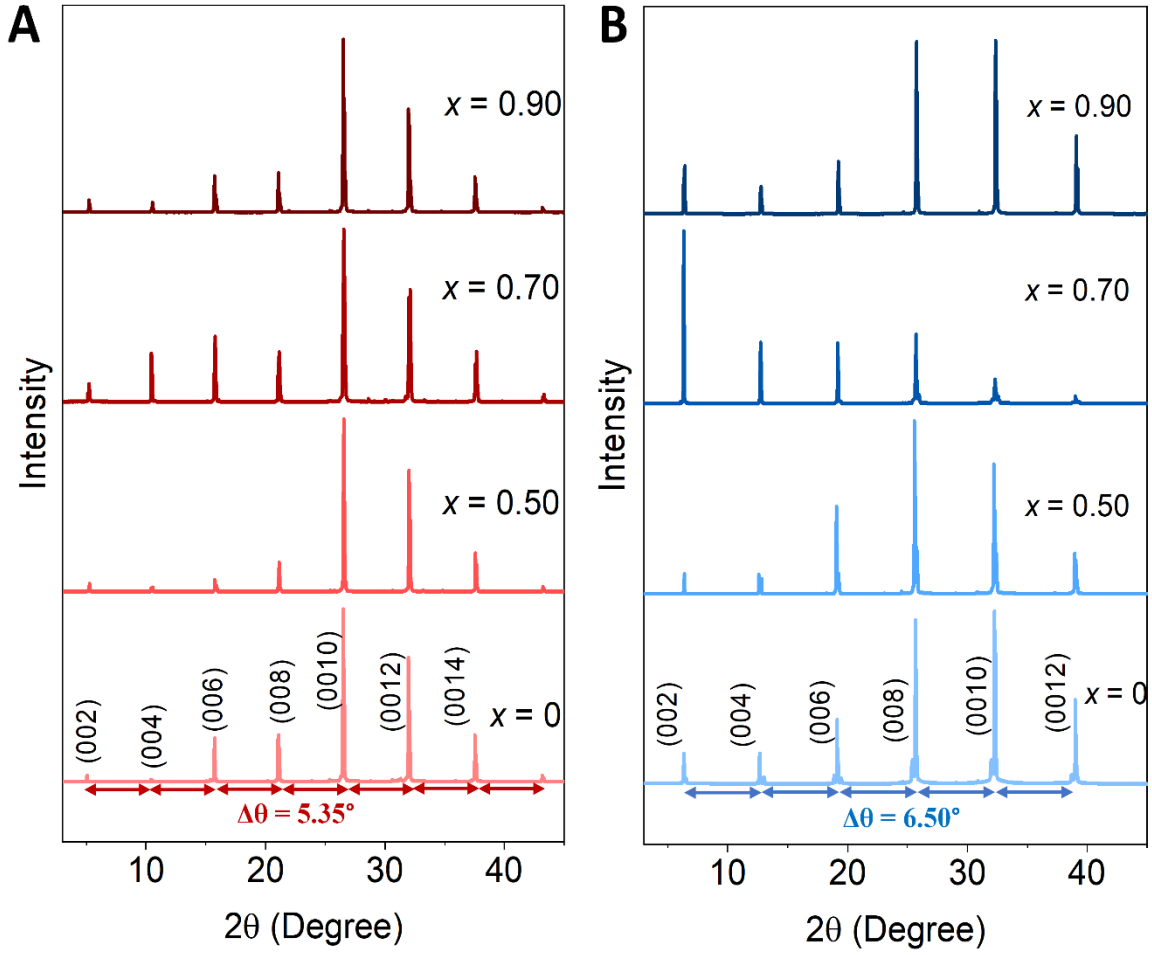

Figure S10. XRD patterns of (A) $(PEA)_2Pb_{1-x}Mn_xBr_4$ crystals and (B) $(BA)_2Pb_{1-x}Mn_xBr_4$ crystals, where x varied from 0 to 0.90.

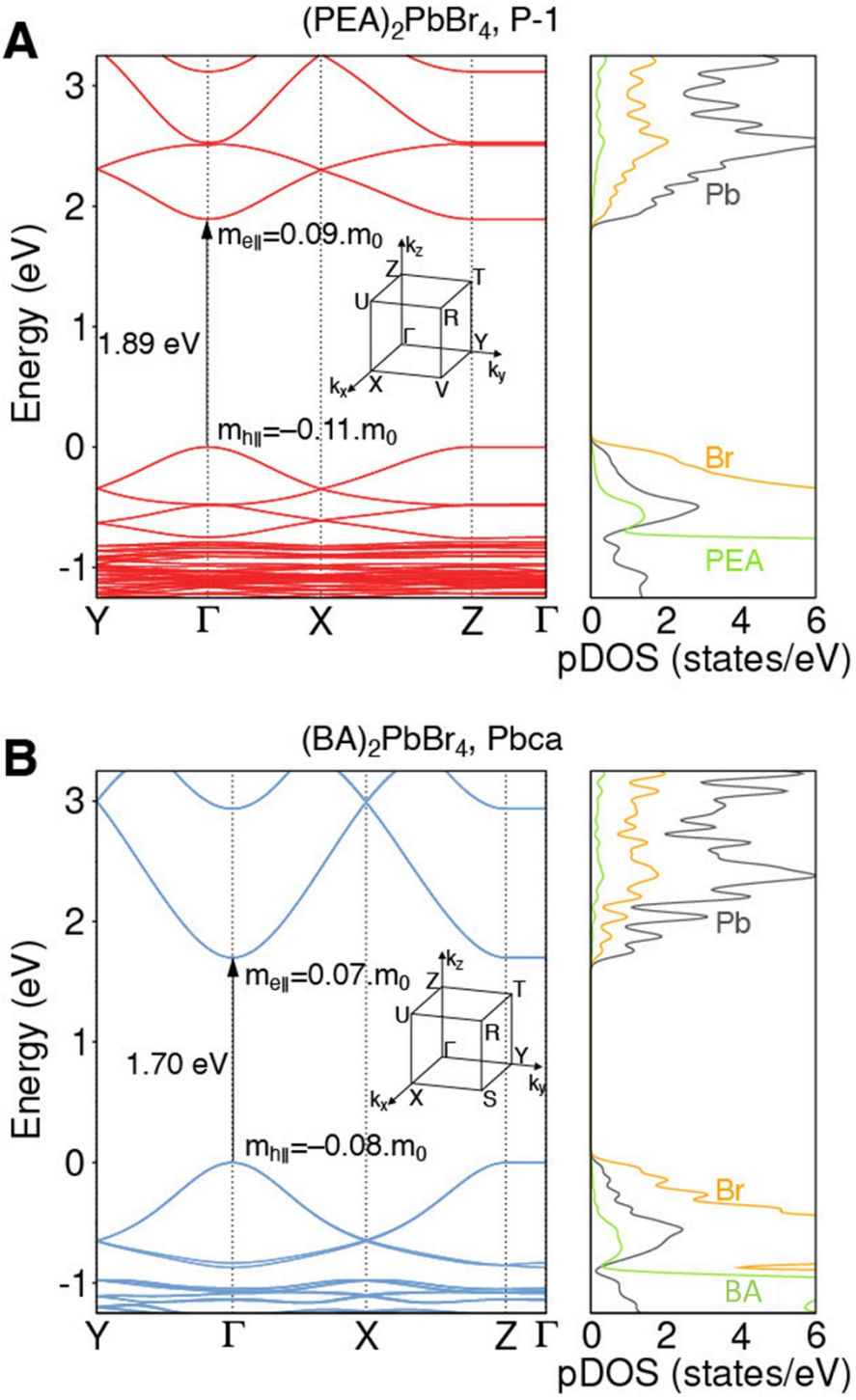

Figure S11. Density functional theory (DFT) computed band structure of (A) $(PEA)_2PbBr_4$ and (B) $(BA)_2PbBr_4$. The right panel of the Figures shows the respective partial density of states (pDOS).

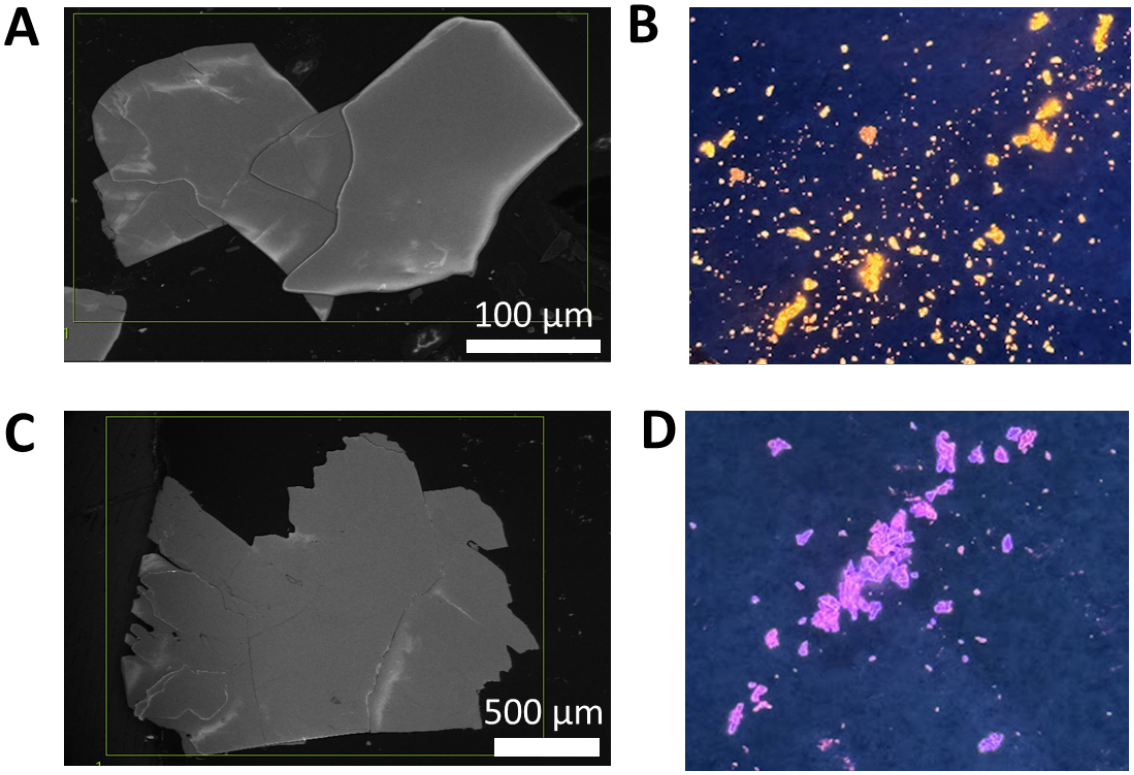

Figure S12. (A, B) SEM and photographic image (under UV 365 nm) of Mn-doped (0.3%) $(PEA)_2PbBr_4$ crystals. (C, D) SEM and photographic image (under UV 365 nm) of Mn-doped (0.3%) $(BA)_2PbBr_4$ crystals. Here, photographic images (under 365 nm UV illumination) of Mn^{2+}-doped PEA- and BA-based crystals are presented to highlight the differences in Mn^{2+} emission at an identical doping level (0.3%).

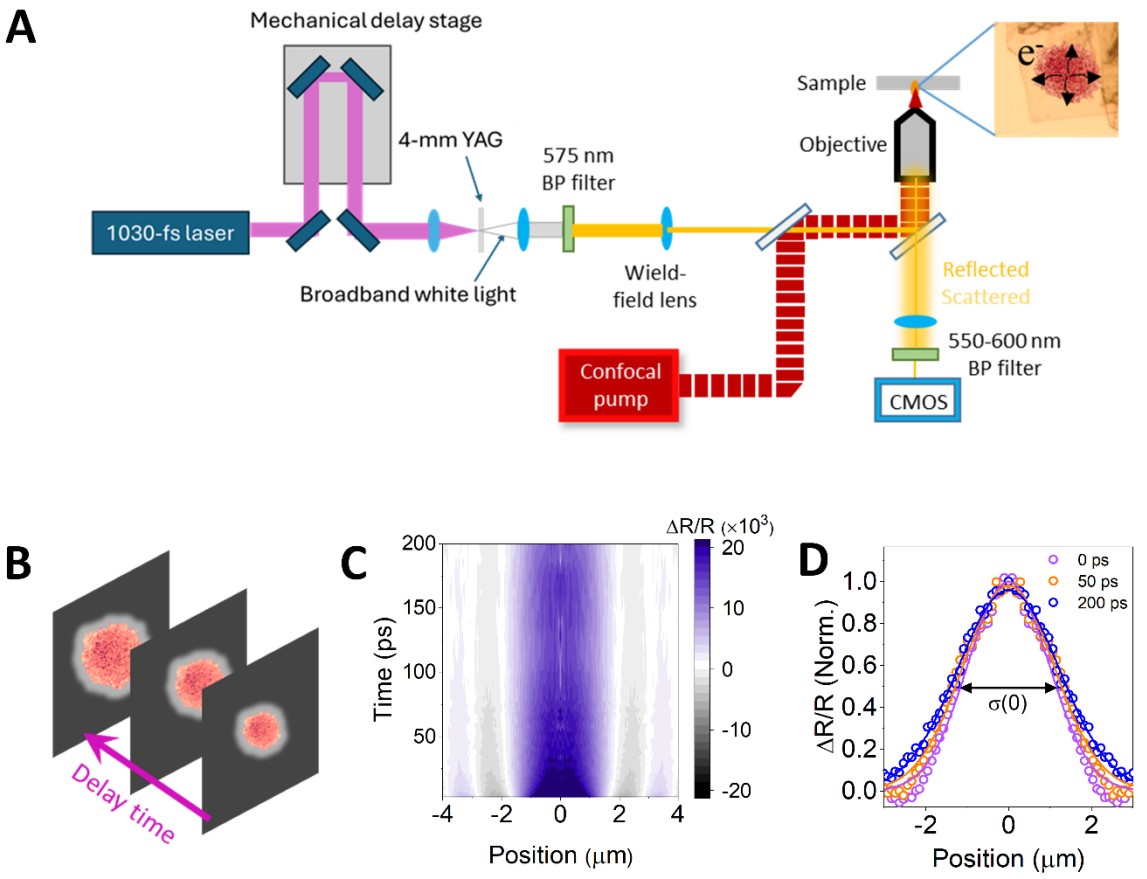

Figure S13. (A) Schematic representation of the experimental setup for pump–probe transient scattering microscopy. (B) Schematic representation of exciton diffusion as a function of pump-probe time delay at the CMOS camera. (C) Diffusion map of the $(BA)_2PbBr_4$ crystal, highlighting the spatial spreading of excitons. (D) Gaussian profiles extracted at different pump–probe delays (0, 50, and 200 ps); the mean square displacement (MSD) of the exciton population over time is calculated from these profiles.

Section 4: References

1. Yadav, A. N. *et al.* Highly Luminescent Manganese-Doped 2D Hybrid Perovskite Nanoplatelets with Dual Emissions Controlled Through Layer Thickness Modulation. *Adv. Opt. Mater.* **12**, (2024).

2. Stoumpos, C. C. *et al.* Ruddlesden-Popper Hybrid Lead Iodide Perovskite 2D Homologous Semiconductors. *Chem. Mater.* **28**, 2852–2867 (2016).

3. Dutta, T. *et al.* Edge versus Interior Mn 2+ Doping in 2D Layered Butylammonium Lead Bromide Perovskite Single Crystals. *J. Phys. Chem. C* **126**, 21109–21116 (2022).

4. Delor, M., Weaver, H. L., Yu, Q. & Ginsberg, N. S. Imaging material functionality through three-dimensional nanoscale tracking of energy flow. *Nat. Mater.* **19**, 56–62 (2020).

5. Seitz, M. *et al.* Exciton diffusion in two-dimensional metal-halide perovskites. *Nat. Commun.* **11**, 1–8 (2020).

6. Soler, J. M. *et al.* The SIESTA method for ab initio order- N materials simulation. *J. Phys. Condens. Matter* **14**, 2745–2779 (2002).

7. García, A. *et al.* S <scp>iesta</scp> : Recent developments and applications. *J. Chem. Phys.* **152**, (2020).

8. Dion, M., Rydberg, H., Schröder, E., Langreth, D. C. & Lundqvist, B. I. Van der Waals Density Functional for General Geometries. *Phys. Rev. Lett.* **92**, 246401 (2004).

9. Cooper, V. R. Van der Waals density functional: An appropriate exchange functional. *Phys. Rev. B* **81**, 161104 (2010).

10. Cuadrado, R. & Cerdá, J. I. Fully relativistic pseudopotential formalism under an atomic orbital basis: spin–orbit splittings and magnetic anisotropies. *J. Phys. Condens. Matter* **24**, 086005 (2012).

11. Troullier, N. & Martins, J. L. Efficient pseudopotentials for plane-wave calculations. *Phys. Rev. B* **43**, 1993–2006 (1991).

12. Artacho, E., S□nchez-Portal, D., Ordej□n, P., Garc□a, A. & Soler, J. M. Linear-Scaling ab-initio Calculations for Large and Complex Systems. *Phys. status solidi* **215**, 809–817 (1999).

13. Murnaghan, F. D. The Compressibility of Media under Extreme Pressures. *Proc. Natl. Acad. Sci.* **30**, 244–247 (1944).